

Article

# Hoek-Brown Failure Criterion-Based Creep Constitutive Model and BP Neural Network Parameter Inversion for Soft Surrounding Rock Mass of Tunnels

Chao Chen, Tianbin Li \*, Chunchi Ma \*, Hang Zhang , Jieling Tang  and Yin Zhang

State Key Laboratory of Geohazard Prevention and Geoenvironment Protection, College of Environment and Civil Engineering, Chengdu University of Technology, Chengdu 610059, China; xchenchaox@126.com (C.C.); zhanghang\_nn720@163.com (H.Z.); tangjieling@stu.cdut.edu.cn (J.T.); zhangyin0503@gmail.com (Y.Z.)

\* Correspondence: ltb@cdut.edu.cn (T.L.); machunchi17@cdut.edu.cn (C.M.)

**Abstract:** This paper summarizes the main factors affecting the large deformation of soft rock tunnels, including the lithology combination, weathering effect, and underground water status, by reviewing the typical cases of largely-deformed soft rock tunnels. The engineering geological properties of the rock mass were quantified using the rock mass block index (*RBI*) and the absolute weathering index (*AWI*) to calculate the geological strength index (*GSI*). Then, the long-term strength  $\sigma_r$  and the elastic modulus  $E_0$  of the rock mass were calculated according to the Hoek–Brown failure criterion and substituted into the creep constitutive model based on the Nashihara model. Finally, the creep parameters of the surrounding rock mass of the Ganbao tunnel were inverted and validated by integrating the on-site monitoring and BP neural network. The inversion results were consistent with the measured convergence during monitoring and satisfied the engineering requirements of accuracy. The method proposed in this paper can be used to invert the geological parameters of the surrounding rock mass for a certain point, which can provide important mechanical parameters for the design and construction of tunnels, and ensure the stability of the surrounding rock mass during the period of construction and the safety of the lining structure during operation.

**Keywords:** tunnel engineering; soft rock; creep parameter; parameter inversion; BP neural network



**Citation:** Chen, C.; Li, T.; Ma, C.; Zhang, H.; Tang, J.; Zhang, Y. Hoek-Brown Failure Criterion-Based Creep Constitutive Model and BP Neural Network Parameter Inversion for Soft Surrounding Rock Mass of Tunnels. *Appl. Sci.* **2021**, *11*, 10033. <https://doi.org/10.3390/app112110033>

Academic Editor: Nikos D. Lagaros

Received: 16 August 2021

Accepted: 19 October 2021

Published: 26 October 2021

**Publisher's Note:** MDPI stays neutral with regard to jurisdictional claims in published maps and institutional affiliations.



**Copyright:** © 2021 by the authors. Licensee MDPI, Basel, Switzerland. This article is an open access article distributed under the terms and conditions of the Creative Commons Attribution (CC BY) license (<https://creativecommons.org/licenses/by/4.0/>).

## 1. Introduction

Tunnel projects in western China often encounter soft rocks with well-developed bedding, such as carbonaceous phyllite, sericite phyllite, schist, carbonaceous slate, sandy slate, and carbonaceous shale. Under high in situ stress, the laminated soft surrounding rock masses are vulnerable to large and rapid deformation and local destruction [1–3]. In these conditions, tunnels frequently suffer from large deformation hazards.

Laminated rock mass, frequently seen in engineering practice and presenting oriented grouped bedding, has more heterogeneous mechanical properties than normal rock mass. Many researchers have developed constitutive models for laminated surrounding rock masses. For instance, Jia et al. [4] applied the microscopic element method with the constitutive model based on damage mechanics and statistical theory to the simulation of rock tunnel stability using the finite element method (FEM). Li et al. [5] developed a three-dimensional creep constitutive model for transversely isotropic rock mass, based on the Burgers viscoelastic model. Li et al. [6] proposed three basic creep patterns of shale and a general methodology for developing the anisotropic creep model. These constitutive models have been used to probe the deformation and failure characteristics of laminated rock masses with varied dip angles. However, research on the constitutive theory of laminated surrounding rock masses in tunnels is fairly limited and cannot provide the theoretical guidance for the engineering design of actual tunnels. In terms of the mechanisms of laminated rock mass deformation, previous studies have mainly

investigated patterns of stability [7], deformation [8–10], mechanical behavior [11], and mechanical properties [12]. The main triggers for large tunnel deformation through highly-dipped laminated soft rock under high in situ stress are high structural stress, unfavorable rock occurrences, and low rock strength [13]. On-site tunnel monitoring has shown that the deformation–failure zone of the surrounding rock mass of laminated soft rock tunnels is concentrated along the direction perpendicular to the rock bedding, instead of the direction of the maximum principal stress; the local deformation of laminated soft rock tunnels is affected by the topography, rock mass structure, and in situ stress [14]. Four mechanisms have been proposed to explain large tunnel deformation, namely, along-bedding sliding, flexural deformation, toppling deformation, and plastic extrusion. For each mechanism, a specific anchoring support plan should be developed [15]. Numerical simulation has been performed to comprehensively analyze the stress environment, the deviator stress distribution [16–19], and the plastic zone distribution [20,21] of the surrounding rock mass during tunnel excavation. Such simulations, incorporating the rock characteristics of deterioration, stabilization, and accelerated creep [22], reveal the characteristics of the surrounding rock mass failure with varied surrounding rock mass strengths, buried depths, and roof strengths [23], which provide guiding values to support the design of the analogous tunnels.

Due to the complexity of geology, geotechnical materials are typically characterized by discontinuity and heterogeneity, and the rheological parameters of the actual surrounding rock mass of the tunnel are often hard to measure. There are two main methods to obtain creep parameters: one is to calculate creep parameters through laboratory testing of rock combined with a creep constitutive model, but there is a large deviation between the laboratory results for rock and on-site rock mass parameters. Second, to obtain the mechanical parameters of the surrounding rock mass through displacement back analysis based on monitoring data [24]. Wenzheng Cao [25] proposed a novel back analysis program based on a BP neural network, which can realize automatic correction and the adjustment of parameters and adapt to most tunnel projects. Qingdong Wu [26] introduced a support vector machine (SVM) and an artificial neural network (ANN) to predict tunnel surrounding rock mass displacement, and compared and analyzed the results of the two methods. Xianghui Deng [27] established a tunnel risk assessment model by combining a fuzzy method with a BP neural network based on historical data from 50 tunnels. Numerical simulation has been widely combined with back-propagation (BP) neural network analysis to calculate the physical and mechanical parameters of surrounding rock mass, which has achieved good application performance [28–30].

This paper proposed a solution for obtaining the creep parameters of the surrounding rock mass in highway tunnels after excavation. First, the long-term strength of the engineering rock mass was obtained using the Hoek–Brown failure criterion, and a creep constitutive model for the rock mass was developed. Then, back-propagation analysis was performed using the on-site monitoring data to obtain the initial values of the creep parameters of the tunnel’s surrounding rock mass. Subsequently, training samples were generated via orthogonal experiments. Then, a BP neural network and numerical simulation were integrated to inversely calculate the tunnel’s surrounding rock mass creep parameters that matched the reality.

## 2. Factors Affecting the Deformation of Soft Rock Tunnels under High In Situ Stresses

The engineering data from some typical largely-deformed soft rock tunnels in China are summarized in Table 1, including the buried depth, formation lithology, in-situ stress, deformation magnitude, and characteristics of deformation and failure.

**Table 1.** Deformation-failure characteristics of tunnels' surrounding rock masses and support structures under complex geological conditions in western China.

Tunnel Name	Tunnel Length /m	Buried Depth /m	Lithology	Max Principal Stress $\sigma_1^{max}$ /MPa	Strength of Rock /MPa	Maximum Deformation /mm	Deformation Characteristics	Strain $\varepsilon$ = Tunnel Closure/Tunnel Diameter $\times 100$
Maoxian Tunnel, Chenglan Railway	25,000	675	Sericite phyllite, carbonaceous phyllite	27.52	1.95	510	Compressive large deformation occurs, with prolonged deformation growth and notable time-dependency; horizontal convergence exceeds crown settlement, due to steep inclination of the surrounding rock mass	8.05
Wuqiaoling Tunnel, Lanxin Railway	20,050	1100	Phyllite, slate	32.8	0.7~2.5	1209	It penetrates the compressive fault; the overall stability of the surrounding rock mass is low; large deformation, early rapid deformation growth, and prolonged duration of deformation are observed due to intensive compression.	9.69
Zhegushan Tunnel, 317 National Rd.	4423	1000	Thin layers of carbonaceous phyllite	17~20	12	300	The relatively large magnitude and prolonged duration of surrounding rock mass deformation are manifested as support breakage, steel arch twisting, and their intrusion into tunnel clearance; the tunnel is prone to collapse.	9.31
Maoyushan Tunnel, Lanyu Railway	8503	700	Thin bedded slate	21.28	5.63	540	Large rapid deformation, with notable rheological effects; severe twisting and fracturing of the steel arch; horizontal convergence far larger than crown settlement	8.94
Gonghe Tunnel, Yusha Expressway	4779	1000	Sandy shale	29.86	11.4	200	Longitudinal cracking and steel frame bending occurs at the initial support of the right spandrel and left arch foot, indicating severe biased compression of the surrounding rock mass	7.52

Surrounding rock masses that are found with large deformations are mostly soft rock with a highly developed bedding texture, such as shale, slate, and phyllite (Table 1). The bedding plane profoundly affects the strength and deformation characteristics of tunnel-surrounding rock mass and is considered the key factor determining the mechanical behavior and deformation-failure characteristics of anisotropic rock mass. In general, the compressional deformation of the surrounding rock mass of tunnels in laminated soft rock occurs mainly at the two sides along the normal direction of the weakest bedding plane. Moreover, the smaller the bedding spacing is, the worse the integrity and self-stabilizing ability of the surrounding rock mass are, which leads to increased proneness to local large deformation and thus a relatively large compressional load on the support structure and highly-deformed lining and surrounding rock mass in local areas. The factors affecting the large deformation of the surrounding rock mass can be summarized as follows:

Based on lithology, the surrounding rock mass can be grouped into two types, namely, plastic and brittle rock. The former consists of soft rock and is typically characterized by low mechanical strength, softening and swelling on wetting, and low slaking resistance, which are all unfavorable for the load-bearing and stability of the tunnel's surrounding rock mass. On the contrary, the latter is of hard rock and generally has a high load-bearing capacity, low softening and swelling tendencies on wetting, and high slaking resistance, which are favorable for the load-bearing and stability of the tunnel's surrounding rock mass. The lithology combination can be generally summarized into four cases, namely, the consistent lithology, hard interbeds (in much softer surrounding rock mass), soft interbeds (in much harder surrounding rock mass), and soft–hard alternating lithology. Different lithology combinations are associated with varied deformation strengths. A soft interbed in the surrounding rock mass is equivalent to a weak part in the surrounding rock mass. In most cases, deformation-failure occurs first in the soft interbed during tunnel excavation. If a hard interbed exists in the surrounding rock mass, it will often suppress the rock deformation, due to its more rigid mechanical properties than those of the surrounding rock mass. Therefore, the deformation magnitude is often relatively small at the hard interbed.

The weathering effect is a common geological phenomenon in nature, which can weaken the cementation between rock particles, form damage cracks, reduce surface roughness, and worsen the physical and mechanical properties of rock. Rapid weathering of soft rock in tunnels will reduce the stability of the surrounding rock mass and affect the safety of the tunnel construction. After the tunnel excavation, the weak layered surrounding rock mass will form internal cracks due to the unloading effect; then, an effective seepage channels are formed, groundwater seeps through these channels, reducing the effective stresses and thus the shear strength along discontinuities and therefore the strength of the rock mass. Therefore, the presence of underground water makes the rock mass more prone to large deformation. The varied underground water seepage pathways or inconsistent thickness of the broken rock zone in the surrounding rock mass after excavation may result in local large deformation of the surrounding rock mass.

Due to the complex geological conditions outlined above, obvious asymmetry is observed for the deformation occurring at the two sides of the central axis, crown, and inverted arch, and local deformation is a common phenomenon for the practice of tunnel engineering. Therefore, it is necessary to quantitatively analyze the engineering geology of each part of the tunnel's surrounding rock mass and accurately invert the creep parameters at each local point from the on-site deformation monitoring data, so as to guide the design and construction of tunnels.

### **3. Rock Strength and Creep Constitutive Model Based on the Hoek–Brown Failure Criterion**

The classic rock mass failure criterion considers rock as a continuous homogeneous medium, which greatly simplifies the reality. A constitutive model for the rock mass with multiple structural planes was developed via superimposition of the constitutive equations of the rock mass with a single joint, which cannot accurately capture the complex

mechanical characteristics of the tiny fissures and multiple groups of structural planes in the rock mass [31,32]. Hence, the semi-empirical semi-theoretical approach was used to characterize the laminated rock mass in engineering practice.

In 1980, E. Hoek and E. T. Brown derived the correlation expression among the limiting principal stresses for the failure of rock (mass) (namely, the Hoek–Brown failure criterion) via a trial-and-error process, based on the statistical analysis of massive data from rock triaxial tests and field testing of rock mass, and the Griffith theory. Then, E. Hoek further proposed the generalized Hoek–Brown empirical failure criterion. The Hoek–Brown empirical failure criterion can reflect the effects of various factors of the rock mass—such as the rock strength, the number of structural planes, and the in situ stress—on the rock mass strength, and overcome the disadvantages of the conventional theoretical equation. The generalized Hoek–Brown failure criterion can be expressed as below:

$$\sigma_r = \sigma_3 + \sigma_c \left( m_b \frac{\sigma_3}{\sigma_c} + s \right)^a \quad (1)$$

where  $\sigma_r$  is the maximum principal stress when the rock fails, namely, the rock strength;  $\sigma_3$  is the minimum principal stress when the rock fails;  $\sigma_c$  is the uniaxial compressive strength of the intact rock;  $m_b$ ,  $s$ , and  $a$  are all empirical parameters;  $m_b$  represents the hardness of the rock, with a value of 0.0000001–25 (0.0000001 for severely-disturbed rock and 25 for intact hard rock);  $s$  represents the broken degree of the rock mass, with a value of 0–1 (zero for completely broken rock and one for intact rock);  $a$  is related to the rock mass quality.

For rock mass with good quality, its strength characteristics are mainly controlled by the rock particle strength, due to the tight packing of rock particles. The restricted Hoek–Brown empirical failure criterion is more applicable to this case and  $a = 0.5$ . On the contrary, for rock mass with poor quality, the packing of fragments in the rock mass is loosened by shearing or weathering, which results in loss of the tensile strength of the rock mass (zero cohesion). Under such circumstances, if there is no confinement, the rock mass will collapse and  $a$  should be assigned to other values. The expressions of the parameters in Equation (1) are listed below:

$$m_b = m_i \exp\left(\frac{GSI - 100}{28 - 14D}\right) \quad (2)$$

$$s = \exp\left(\frac{GSI - 100}{9 - 3D}\right) \quad (3)$$

$$a = \frac{1}{2} + \frac{1}{6} \left( e^{-GSI/15} - e^{-20/3} \right) \quad (4)$$

$$0 < \sigma_3 < \frac{\sigma_c}{4} \quad (5)$$

where  $D$  is the disturbance factor (zero for the undisturbed rock mass, and one for completely disturbed rock mass).  $m_i$  indicates the values of constants for intact rock, which can be determined by laboratory testing (uniaxial compression test and conventional triaxial compression test). Based on laboratory data and engineering experience, E. Hoek et al. [33,34] developed a comprehensive and detailed  $m_i$  value table that was able to cover a variety of rocks; the  $m_i$  index of intact phyllite in this paper refers to this  $m_i$  value table.

Afterwards, E. Hoek and E. J. Brown further derived the estimations of the relevant mechanical parameters of the rock mass [35], based on Equation (1):

$$\sigma_{cr} = \sqrt{s} \sigma_c \quad (6)$$

$$\sigma_{tr} = \frac{1}{2} \sigma_c \left( m_b - \sqrt{m_b^2 + 4s} \right) \quad (7)$$

$$E_{rm} = 10^5 \frac{1 - D/2}{1 + \exp[(75 + 25D - GSI)/11]} \quad (8)$$

Equation (1) shows that the *GSI* value is the key to determining the mechanical parameters of the Hoek–Brown failure criterion for the rock mass. However, E. Hoek proposed only a general range for the texture type and weathering conditions of the rock mass and offered no quantitative calculation method.

Rock quality designation (*RQD*) is the most commonly used index to describe the structural characteristics of rock mass, which is defined as the percentage of the sum of the lengths of intact core pieces longer than 0.1 m relative to the chosen length of an evaluated drill core ( $RQD = (\frac{\text{the lengths of intact core pieces} \geq 10 \text{ cm per footage}}{\text{the length of an evaluated drill core}} (\%))$ ); however, the definition of *RQD* requires that the quality of core pieces must be “hard and sound”, meaning it can only calculate the percentage of the core with a length beyond 10 cm in the total cored length, which is not suitable for integrity evaluations when characterizing the multi-joint rock mass.

This paper introduces the rock mass block index (*RBI*) and the absolute weathering index (*AWI*) to quantify the *GSI*. The *RBI*, proposed by Hu et al. [36], can thoroughly characterize the block dimension, texture type, and structural packing of blocks for the rock mass. The *RBI* defines the percentages of drilling cores with the measured lengths of 3–10 cm, 10–30 cm, 30–50 cm, 50–100 cm, and >100 cm as the weights, and the value of the *RBI* is the sum of the weights multiplied by the corresponding coefficients.

Although the rock mass has the same *RQD* value, the *RBI* values can be different. For example, the rock mass of *RQD* = 90% can be 10~30 cm with a mosaic structure, or 30~50 cm with a block structure, or 50~100 cm with a block structure, or even more than 100 cm with intact structure. Under the same *RQD*, the larger the *RBI* is (from a mosaic structure to an intact structure), the more intact the rock mass is, and the *RBI* can be regarded as an extension of *RQD*. The calculation formula of *RBI* is shown below:

$$RBI = 3C_{r3} + 10C_{r10} + 30C_{r30} + 50C_{r50} + 100C_{r100} \quad (9)$$

where  $C_{r3}$ ,  $C_{r10}$ ,  $C_{r30}$ ,  $C_{r50}$ , and  $C_{r100}$  are the acquisition rates (weights in percentages) of the cores with the lengths of 3–10 cm, 10–30 cm, 30–50 cm, 50–100 cm, and >100 cm, respectively. The details of the rock mass texture representation by *RBI*, associated with the field description, are shown in Table 2.

**Table 2.** Representation of rock mass textures by *RBI*.

Texture Type	<i>RBI</i>	Rock Mass Characteristics
Laminated mosaic texture	30–10	Relatively intact, barely, or partially disturbed, often developing 3 groups of structural planes with the spacing of 30–50 cm
Mosaic texture	10–3	Less intact, mostly disturbed, broken yet with tightly packed fragments, generally developing 3–4 groups of structural planes with the spacing of 10–30 cm
Broken texture	3–1	Broken rock mass, sufficiently disturbed, composed of fragments or thin layers, with extensive structural planes presenting spacing generally smaller than 10 cm
Loose texture	1–0	Extremely crushed rock mass, extremely disturbed, composed of loose rock blocks, and angular fragments with crushed debris

The mechanical properties of rock are also related to the weathering level. Chemical weathering can alter the mineral composition of rock and thus alter its physical and mechanical performance.

Parker [37] proposed an index of weathering for silicate rocks, based on the proportions of the alkali and alkaline earth metals present. The bond strengths of the most mobile of the major elements with oxygen are used as weighting factors in the index; the proposed index is defined by the following expression:

$$WI = \left[ \frac{a(\text{Na})}{0.35} + \frac{a(\text{Mg})}{0.9} + \frac{a(\text{K})}{0.25} + \frac{a(\text{Ca})}{0.7} \right] \times 100 \tag{10}$$

where  $a(X)$  ( $X = \text{Na}, \text{Mg}, \text{K}, \text{Ca}$ ) indicates the atomic proportion of element  $X$ , defined as the atomic percentage divided by the atomic weight, and the denominator is the bond strength of element  $X$  with oxygen, which represents the stability of the element in the weathering process. From fresh rock to weathered rock, the index  $WI$  is gradually reduced.

The weathering index of rock mass  $AWI_0$  [38] can be expressed as below:

$$AWI_0 = WI/WI' \tag{11}$$

where  $WI$  stands for the weathering index of the weathered rock, whereas  $WI'$  represents that of the fresh rock. Thus, a higher value of  $AWI$  indicates fresher rock with a lower level of chemical weathering and correspondingly better mechanical properties. On the contrary, a higher  $AWI$  value denotes a high level of chemical weathering. Obviously,  $AWI$  quantitatively characterizes the weathering conditions of the engineering rock mass. Based on the research on the relationship between the weathering index and the weathering level of the rock [39], the weathering level of rock based on  $AWI$  is shown in Table 3/ Figure 1. In order to conveniently determine the absolute weathering index  $AWI_0$  of the rock mass, can use the ratio of uniaxial compressive strength of fresh rock to weathered rock.

**Table 3.** Representation of the rock mass weathering characteristics by  $AWI$ .

Weathering Condition	$AWI_0$	Weathering Characteristics
Non-weathered	>0.90	Very good fracture surface: very coarse, fresh, indicating well-sealed fresh rock matrix and no weathering
Slightly weathered	0.90–0.75	Good fracture surface: coarse, relatively fresh, with the presence of rugh and the slight alteration of minerals with low weathering resistance, indicating slight weathering
Weakly weathered	0.75–0.55	Ordinary fracture surface: smooth with no filling, partial alteration of minerals with low weathering resistance, indicating weak weathering
Intensively weathered	0.55–0.35	Poor fracture surface: the presence of slickensides, covering of tight films or filling of angular debris on the surface, high alteration of minerals with low weathering resistance, indicating intensive weathering
Extremely weathered	≤0.35	Very poor fracture surface: the presence of slickensides, and soft clay films or clay filling; the vast majority of minerals with low weathering resistance are altered; indicating extreme weathering

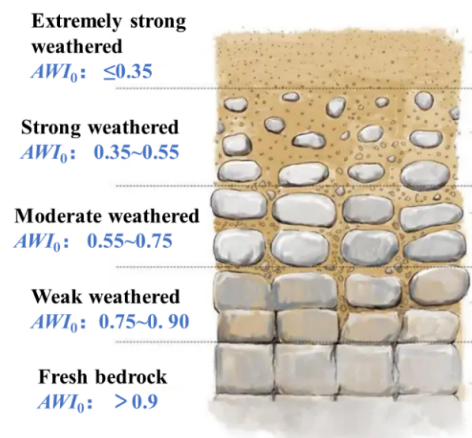


**Figure 1.** Schematic diagram of rock weathering.

A correction factor  $\lambda$  is introduced to describe the effects of underground water on the weathering conditions of the jointed rock mass (Table 4). Accordingly, the rock mass weathering index, considering the effects of underground water, can be expressed as  $AWI = \lambda AWI_0$ .

**Table 4.** Recommended values for the correction factor  $\lambda$  to capture the effects of underground water on the weathering conditions of rock mass.

Production Status of Underground Water	RBI Values of Jointed Rock Mass			
	30–10	10–3	3–1	1–0
Humid or dripping	0.95	0.95–0.89	0.89–0.83	0.83–0.76
Rain-like or spring-like production with water pressure < 0.1 MPa; or unit water production rate < 10 L/min·m	0.95–0.89	0.89–0.83	0.83–0.76	0.76–0.71
Rain-like or spring-like production with water pressure > 0.1 MPa; or unit water production rate > 10 L/min·m	0.89–0.83	0.83–0.76	0.76–0.71	0.71–0.67

By integrating the quantitative indexes in Tables 2–4 for the texture and weathering conditions of the rock mass, the geological strength index (GSI) quantification method (Figure 2) can be obtained.

Rock Texture and Quantification	Weathering Intensity Evaluation and Quantification																		
	Very good: very coarse, fresh, and no weathering $1.00 \geq AWI > 0.90$				Good: coarse, slightly weathered, and with rust on the surface $0.90 \geq AWI > 0.75$			Ordinary: smooth, and weakly weathered or altered $0.75 \geq AWI > 0.55$				Poor: the presence of slickensides, intensively weathered, with tight film covering or filling of angular debris $0.55 \geq AWI > 0.35$			Very poor: the presence of slickensides, extremely weathered, with soft clay films or clay filling $AWI \leq 0.35$				
	AWI=1.0	AWI=0.975	AWI=0.95	AWI=0.925	AWI=0.9	AWI=0.85	AWI=0.80	AWI=0.75	AWI=0.7	AWI=0.65	AWI=0.6	AWI=0.55	AWI=0.50	AWI=0.45	AWI=0.40	AWI=0.35	AWI=0.30	AWI=0.25	RBI=20
Blocky: undisturbed rock mass with good mosaic packing, developing three groups of orthogonal discontinuous intersecting structural planes and composed of cubic rock blocks $30.0 < RBI \leq 10.0$					70														RBI=26
								60											RBI=22
												50							RBI=18
															40				RBI=14
Crushed: partially disturbed rock mass with mosaic packing, developing four or more groups of discontinuous intersecting structural planes that result in angular rock blocks $10.0 < RBI \leq 3.0$															30				RBI=10
																	20		RBI=9
																			RBI=7
Blocky/disturbed: developing multiple groups of discontinuous intersecting structural planes that result in angular rock blocks; undergone folding and (or) faulting $3.0 < RBI \leq 1.0$																			RBI=5
																			RBI=3
Discrete: extremely crushed rock mass with loose mosaic packing of rock blocks, composed mixed various rock debris, or angular and round rock blocks $RBI \leq 1.0$																			RBI=2
																			10

**Figure 2.** GSI quantification of rock mass [31]. Note: The following example is used to demonstrate how to use the above table. In the case of  $AWI = 0.52$  and  $RBI = 9.7$ , two vertical and horizontal lines are drawn according to the index values (the dashed lines in the table); the intersection point is found between 40 and 45; the GSI value at the point is calculated via linear interpolation (the result is 41).

The widely applied Nishihara model can characterize the decelerating, steady-state, and accelerating creep phases of rock. Extensive experiments have shown that notable damage of the rock occurs only in the accelerating creep phase. The rock strength  $\sigma_r$ , presented upon the failure of the rock, is the long-term strength for rock creep. The creep elements of the rock mass model are shown in Figure 3.

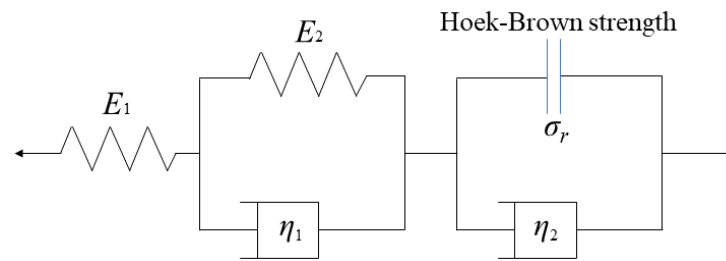


Figure 3. Combination of the creep elements for rock mass.

The creep equation can be expressed as below:

$$\varepsilon = \begin{cases} \frac{\sigma}{E_0} + \frac{\sigma}{E_1} \left[ 1 - \exp\left(-\frac{E_1 t}{\eta_1}\right) \right] & (\sigma \leq \sigma_r) \\ \frac{\sigma}{E_0} + \frac{\sigma}{E_1} \left[ 1 - \exp\left(-\frac{E_1 t}{\eta_1}\right) \right] + \frac{\sigma - \sigma_r}{\eta_2} t & (\sigma > \sigma_r) \end{cases} \quad (12)$$

where  $E_0$  is the elastic modulus;  $E_1$  is the viscoelastic modulus;  $\eta_1$  and  $\eta_2$  are the viscosity coefficients;  $\sigma$  is the load stress;  $\varepsilon$  is the total strain;  $\sigma_r$  is the long-term strength calculated using Equation (1) (the Hoek–Brown failure criterion); and  $t$  is the creep time.

The strength parameters of the laminated jointed rock mass at each position (Figure 4) can be obtained according to the Hoek–Brown failure criterion. Then, they are input into the numerical simulator via the creep constitutive model (Equation (12)) to calculate the deformation of the surrounding rock mass (Figure 5).

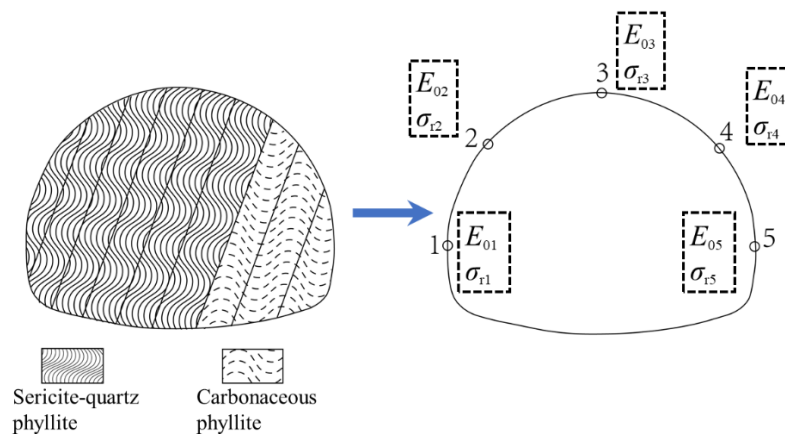


Figure 4. Surrounding rock mass strength parameters based on the Hoek–Brown failure criterion.

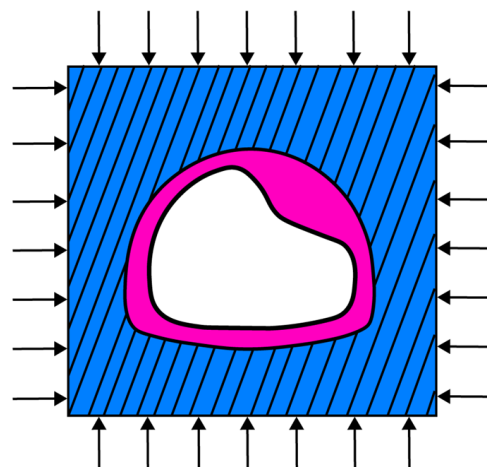
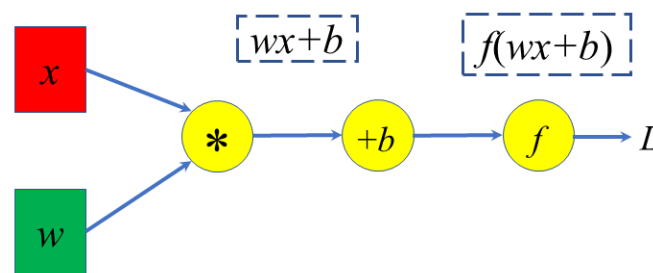


Figure 5. Schematic diagram of the surrounding rock mass deformation.

#### 4. Field Application

The stress state of the surrounding rock mass changes after starting the excavation of the tunnel. Hence, the support design based on the surrounding rock mass parameters obtained in the previous investigation is inappropriate, in particular for a tunnel engineering design with a high buried depth, large span, and highly-developed structural planes. To provide a basis for theoretical reference and design, this paper inverts and validates the surrounding rock mass parameters by integrating the on-site monitoring with a BP neural network.

The BP neural network is a typical nonlinear algorithm, composed of the input, output, and several (one or more) hidden layers (Figure 6), and each layer has several nodes. The connection of nodes between layers is represented by the weight. The BP neural network with one hidden layer is the traditional shallow neural network, whereas that containing multiple hidden layers is the deep learning neural network (Figure 7).



**Figure 6.** Schematic diagram of the BP neural network structure. Note: The weight  $w$  represents the connection strength; the bias  $b$  indicates whether or not the node is easy to activate (threshold).

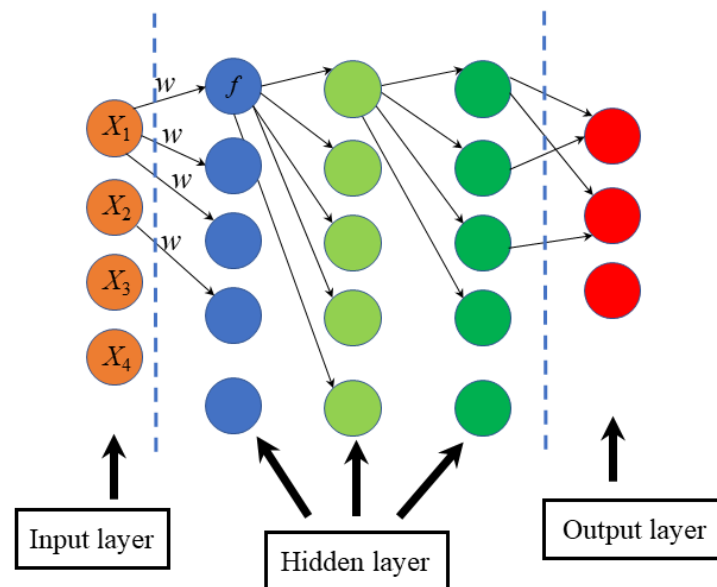


**Figure 7.** Deep BP neural network structure.

The core steps for training the BP neural network are illustrated below (Figure 8), in which the solid line represents forward propagation and the dashed line represents back propagation. The forward propagation means that the data (information or signal) are first imported into the input end, delivered along the network direction, and multiplied by the corresponding weight. The products of the input data and the corresponding weights are then summed, and the results are input into the activation function for calculation. Then calculation results are delivered to the next node as the input. The calculation is performed successively until the final output is obtained.

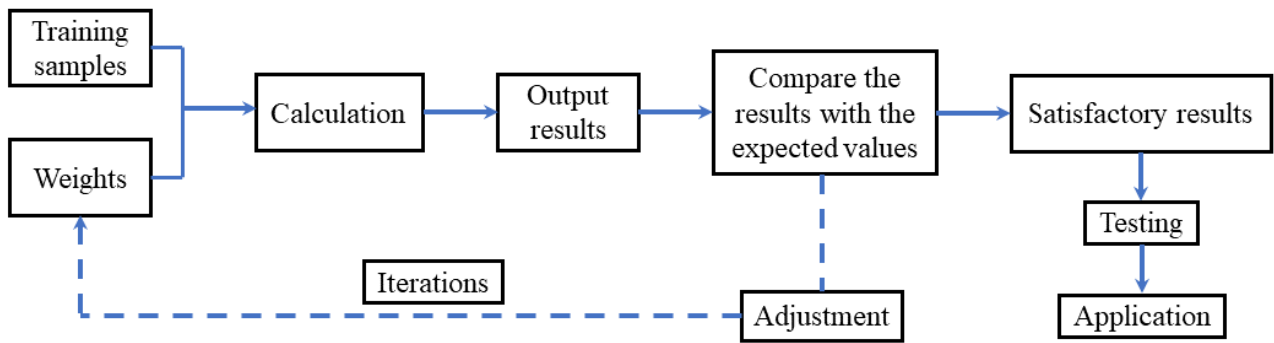


Figure 8. Steps for training the BP neural network.

Here we summarize the inversion workflow of the creep parameters of the surrounding rock mass, as shown below (Figure 9).

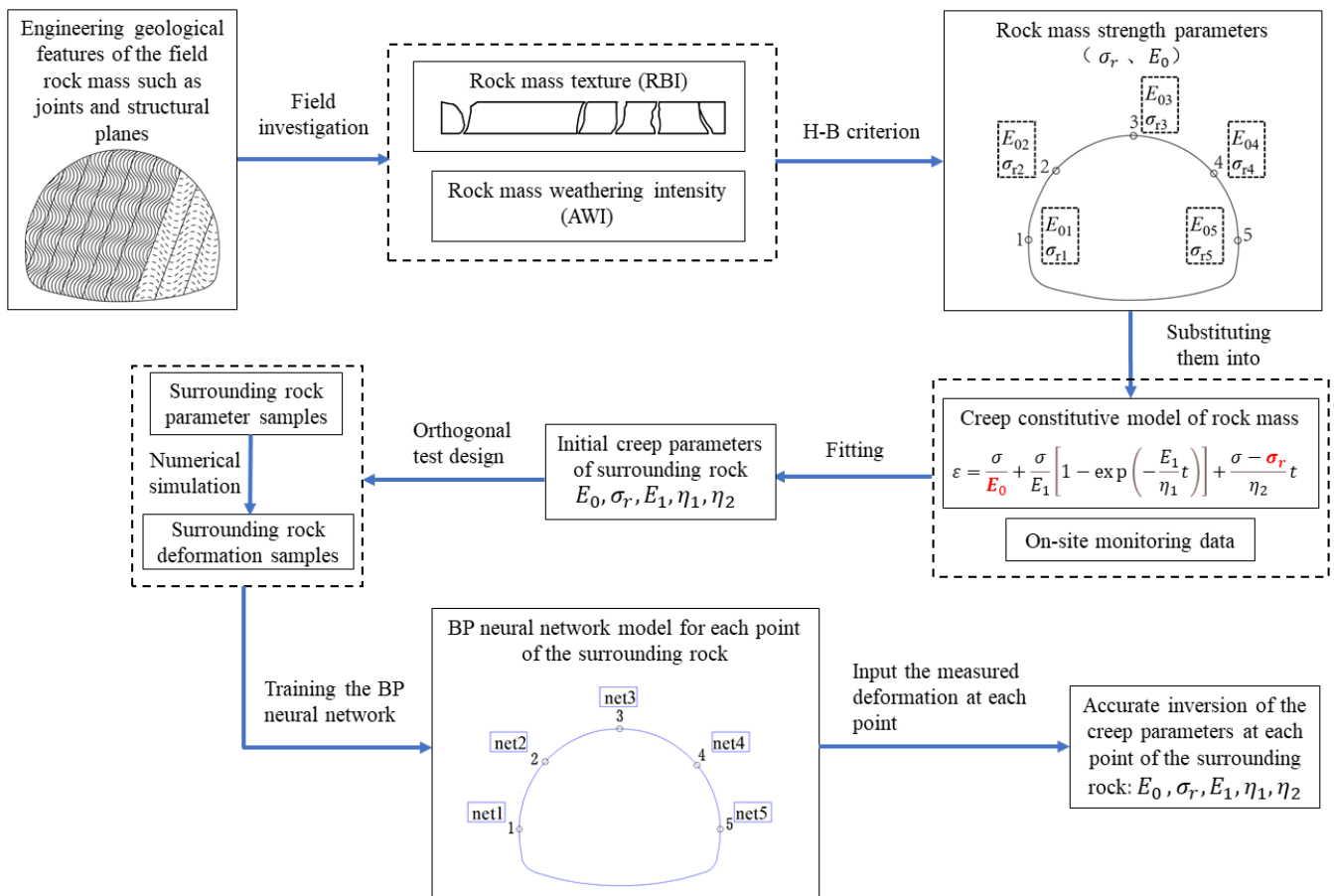


Figure 9. Inversion workflow for the creep parameters of the surrounding rock mass.

The Ganbao tunnel project of the Wenchuan–Maerkang expressway was taken as an engineering case study. It is an ultra-long left-right separated tunnel project (the left tunnel is 4777 m long and the right one is 4796 m long). The longitudinal profile of the tunnel is illustrated in Figure 10, in which the red surrounding rock mass mainly represents the sericite phyllite; the yellow part represents the sericite phyllite interbedded by carbonaceous phyllite and metasandstone; the blue part shows the carbonaceous phyllite and sericite phyllite interbedded by metasandstone; the green part represents the sericite phyllite and carbonaceous phyllite; and the black part indicates the carbonaceous phyllite. The tunnel was excavated using the drilling and blasting method. A large deformation occurs

at the mile sections K141 + 540~K141 + 860 and K143 + 485~K143 + 650, which results in the circumferential cracking of multiple points along the initially supported arch and local cracking and spalling of the sidewall and tunnel crown (Figure 11). The monitoring section is located at K143 + 621 and starts monitoring after 12 h of excavation. The overburden near the monitoring section consists of collapsed debris deposits, sericite phyllite and carbonaceous phyllite (from top to bottom, Figure 12), the lithology presented on the face of the surrounding rock mass of the largely-deformed tunnel section (Figure 13) is dominated by the carbonaceous phyllite and sericite phyllite, mainly the Grade-V surrounding rock mass. The rock mass is found with a laminated texture and has a buried depth of 646 m, with a vertical stress of 21.7 MPa and a horizontal stress of 8.3 MPa. Field observations indicate minimal effects of underground water, and thus the correction factor  $\lambda$  for the effects of underground water on the weathering conditions of the rock mass is set as one.

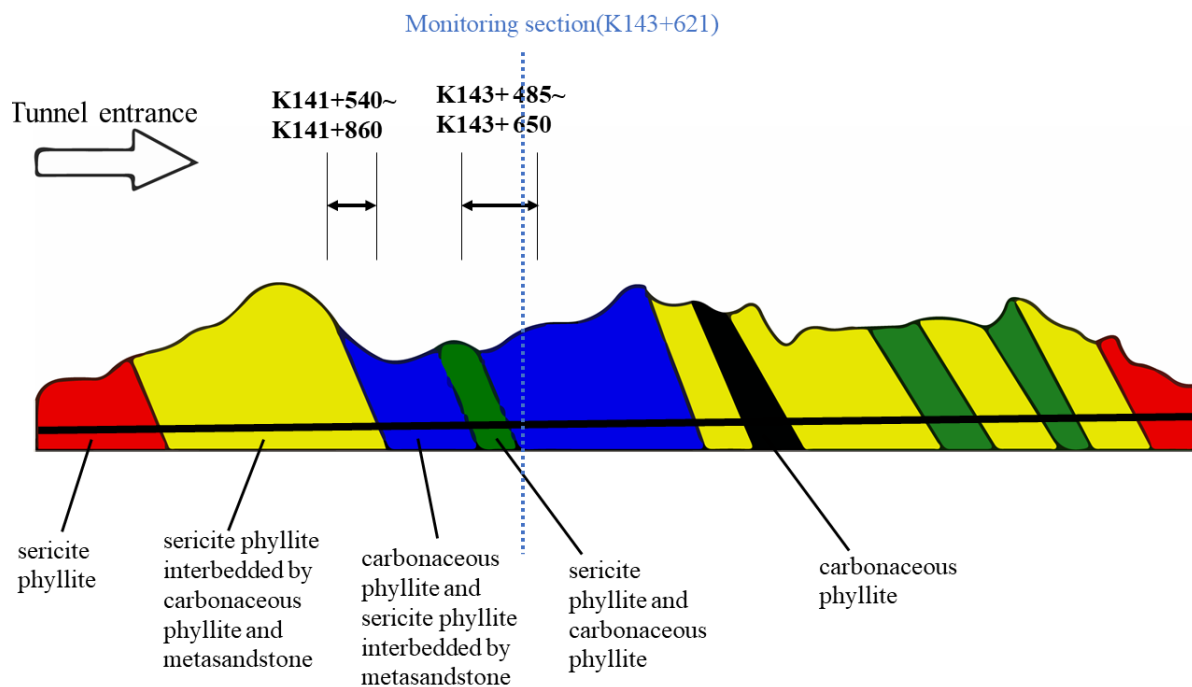


Figure 10. Longitudinal profile of the tunnel.

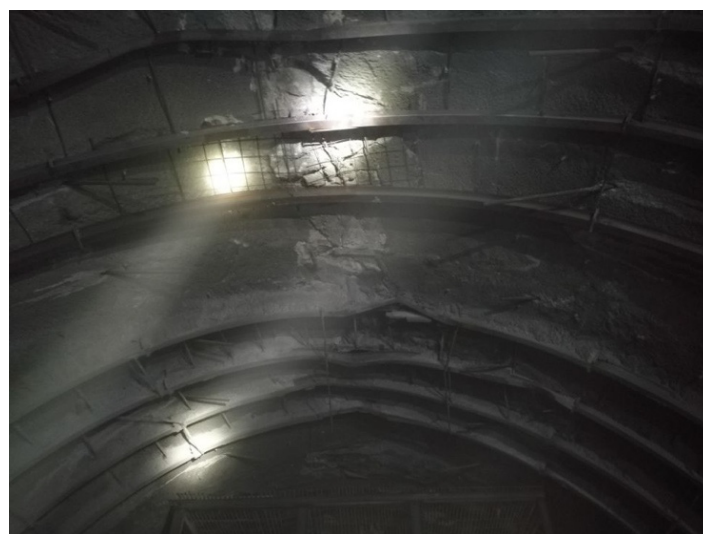


Figure 11. The twisted steel arch and back haunch fillet of the arch, and rockfall of the initial support.

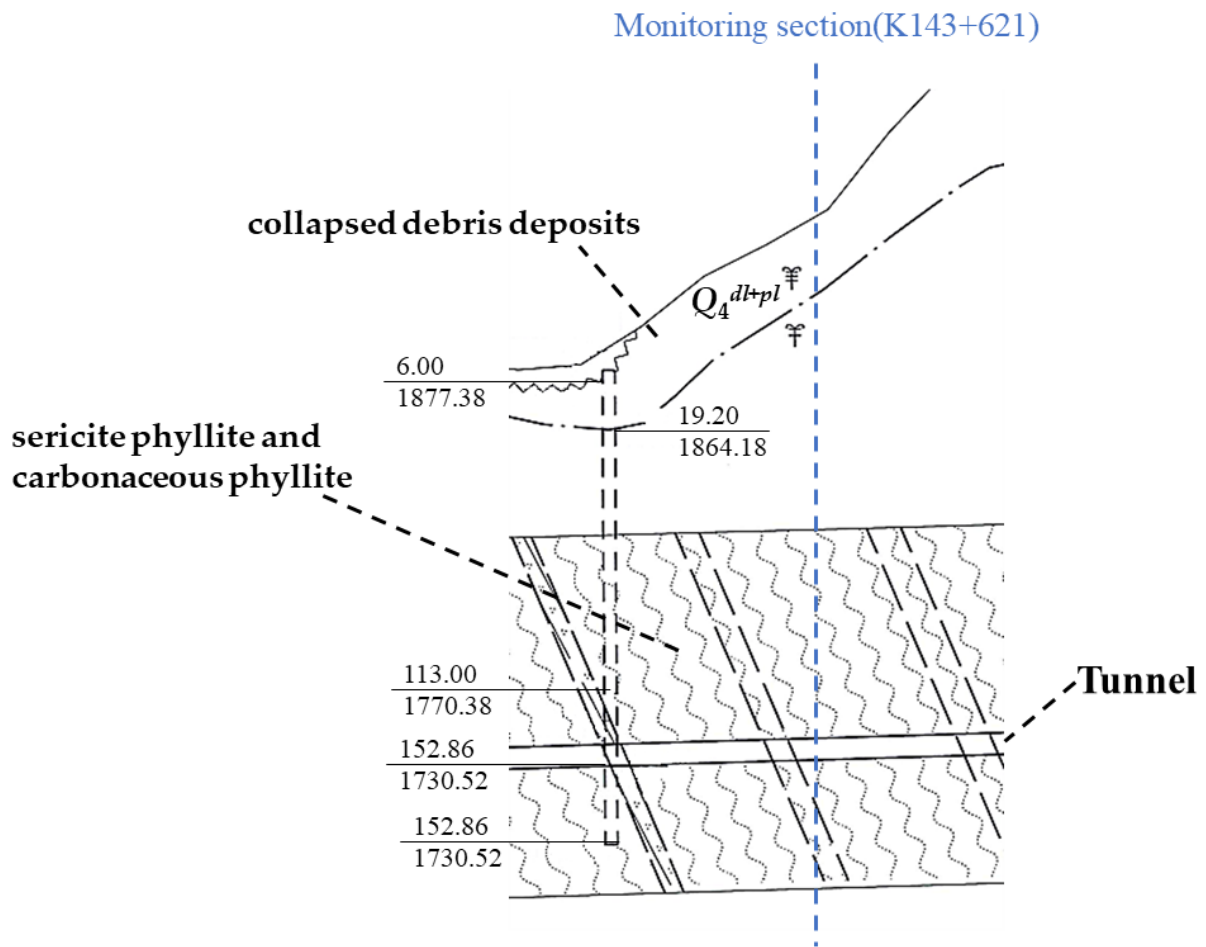


Figure 12. The overburden near monitoring section K143 + 621.

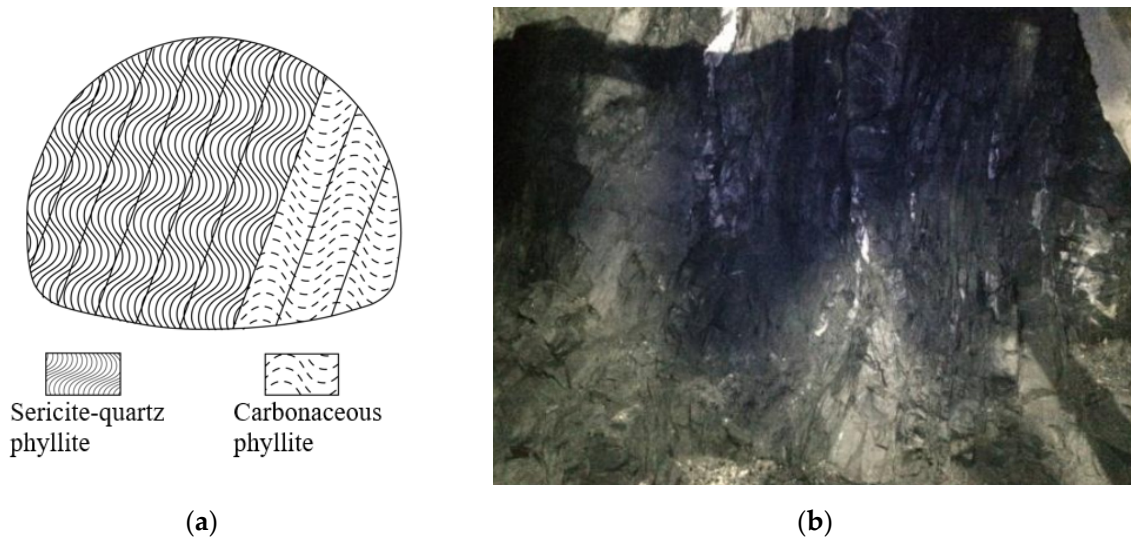


Figure 13. Tunnel face (unexcavated) at K143 + 630. (a) Geological sketch picture. (b) Photo of the tunnel face.

The pre-excitation boreholes are arranged on the tunnel face (Figure 14), the rock cores are collected via pre-excitation boreholes for investigation, and the *RBI* value of rock mass (Table 5) for each borehole is calculated using Equation (9) and the core length measured on site. For the monitoring of surrounding rock mass deformation after excavation, the on-site monitoring point placement is illustrated in Figure 14.

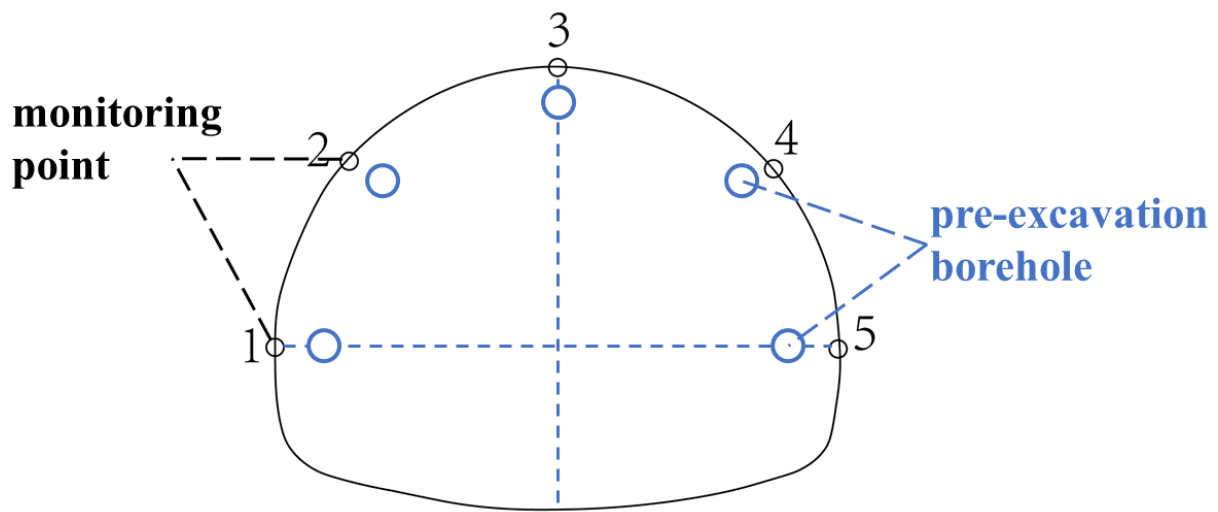


Figure 14. Monitoring point and pre-excitation borehole placement in the tunnel (K143 + 621).

Table 5. Cores collected via pre-excitation boring at each monitoring point and the RBI values.

Monitoring Point	Cores	RBI Values
1		6.763
2		5.626
3		3.748
4		2.8
5		4.331

Taking Point 4 as an example, the field investigation shows that the RBI of the surrounding rock mass cores at Point 4 is about 2.8; the AWI is about 0.65. According to Table 4, the GSI value is 33. For the intact phyllite rock, the Hoek–Brown constant  $m_1 = 10$  and the uniaxial compressive strength  $\sigma_c = 35$  MPa. From Equation (5), we have  $\sigma_{3max} = \frac{\sigma_c}{4} = 8.75$  MPa and from Equations (2)–(4), we have  $m_b = 0.916$ ,  $s = 0.000587$ , and  $a = 0.518$ .

Finally, according to Equation (1), the uniaxial comprehensive strength of the rock mass  $\sigma_r = 16.33$  MPa and the elastic modulus  $E_0 = 1.11$  GPa. The basic parameters at the other points are summarized in Table 6.

**Table 6.** Basic parameters of the surrounding rock mass at each monitoring position.

Monitoring Point	RBI	AWI	GSI	$m_b$	$s$	$a$	$\sigma_r$ (MPa)	$\sigma_3 = \frac{\sigma_c}{4}$ (MPa)	$E_0$ (GPa)
1	6.763	1.570	79.708	2.212	0.001418	0.27	36.8	45.29	2.69
2	5.626	1.306	66.305	1.840	0.001179	0.22	32.28	37.67	2.24
3	3.748	0.870	44.169	1.226	0.000786	0.15	21.57	25.10	1.49
4	2.8	0.65	33	0.916	0.000587	0.11	16.33	18.75	1.11
5	4.331	1.006	51.050	1.417	0.000908	0.17	22.8	29.01	1.73

The fitting of the creep constitutive model (Equation (11)) to the surrounding rock mass monitoring data (Figure 15) was performed using the least square method to calculate the creep parameters of the rock mass at each monitoring point. The calculation results are shown in Table 7.

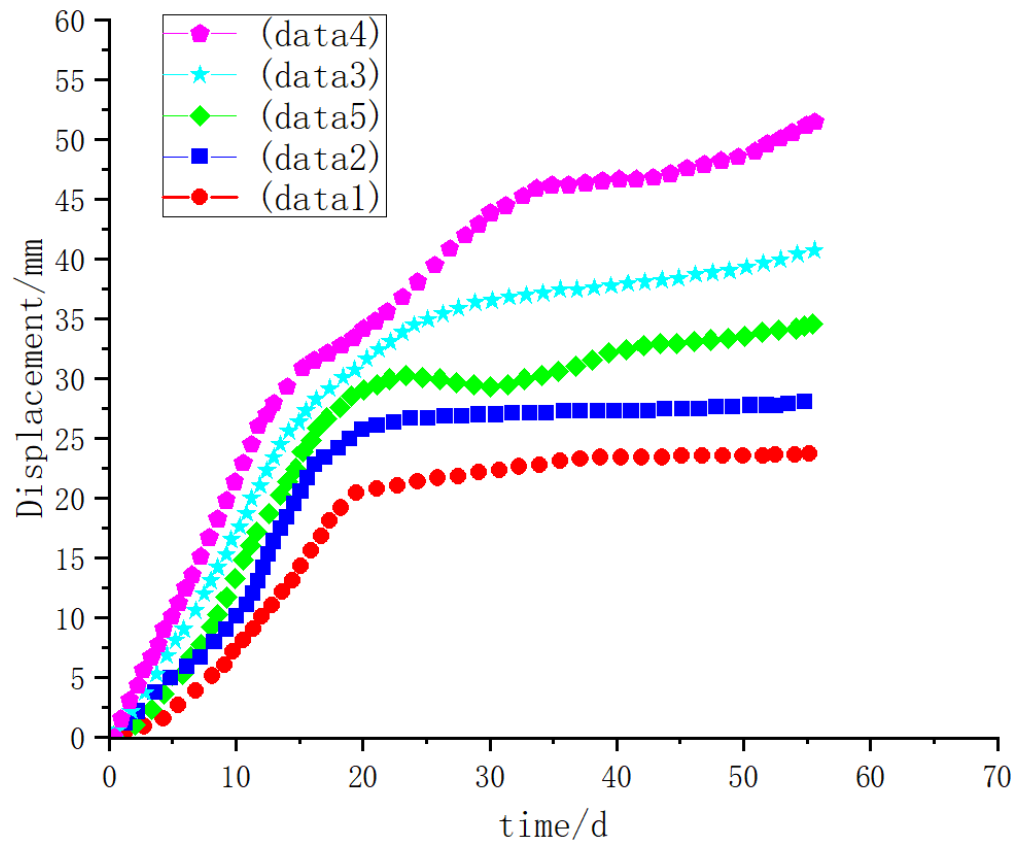


**Figure 15.** Measured displacement vs. time at each monitoring point.

**Table 7.** Creep parameters of the rock mass at each monitoring point.

Point No.	$E_0$ /GPa	$\sigma_r$ (MPa)	$E_1$ /GPa	$\eta_1$ /(GPa·d)	$\eta_2$ /(GPa·d)
1	2.69	36.8	0.8	16.38	93.71
2	2.24	32.28	0.71	11.22	88.63
3	1.49	21.57	0.5	8.78	6.55
4	1.11	16.33	0.4	7.87	5.62
5	1.73	22.8	0.6	10.11	78.52

Since the factors affecting the deformation of the surrounding rock mass are varied in the different positions of the tunnel, a neural network was constructed and trained for each point to improve the inversion accuracy. The single-variable method was used for training, which means when the neural network of one point is being trained, the parameters of the other points are constant. Here, Point 4 was taken as an example to demonstrate the training of the neural network. As stated above, the parameters of the other points were fixed, and the learning sample dataset of the surrounding rock mass mechanical properties was built based on the orthogonal test design (Figure 16). The sample parameters in the training dataset were substituted into the numerical simulation model developed using Midas (Figure 17), and the forward calculation was performed to obtain the surrounding rock mass deformation magnitude at each point (Table 8). We used 80% of the data in Table 8 as the training dataset, whereas we used the other 20% as the testing dataset.

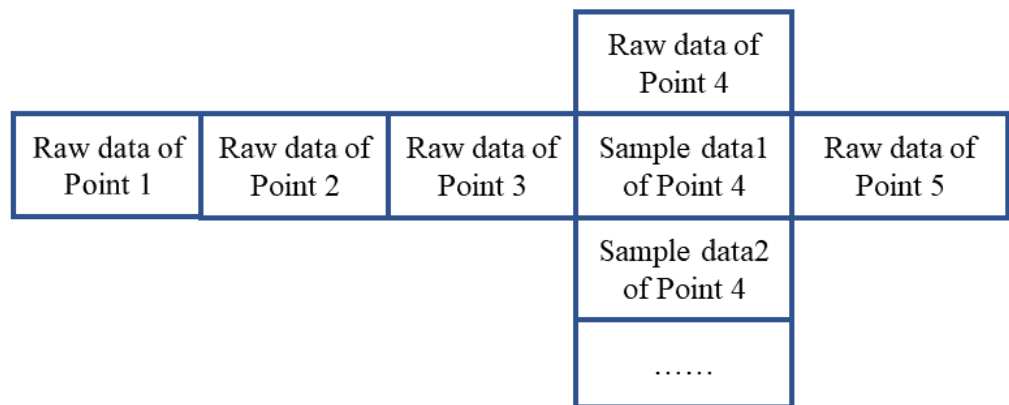


Figure 16. Training the dataset at a certain point in a single-variable approach.

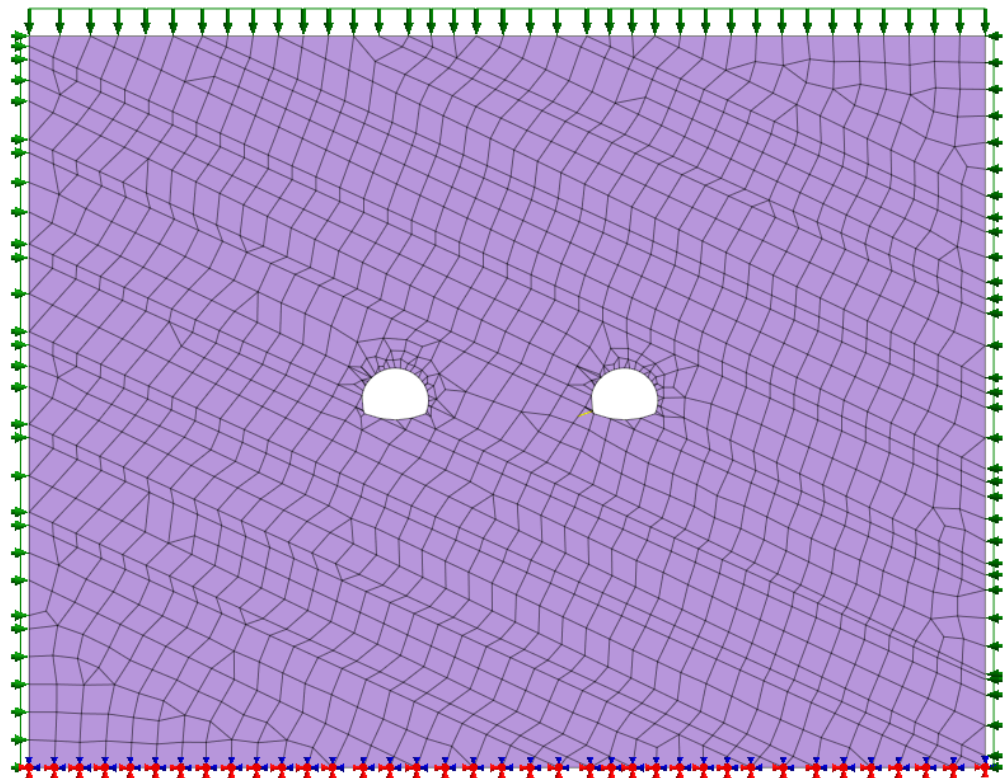


Figure 17. Numerical simulation model of the tunnel.

**Table 8.** The orthogonal test design plan and calculation results for Point 4.

No.	$E_0$ /GPa	$\sigma_r$ /MPa	$E_1$ /GPa	$\eta_1$ /(GPa·d)	$\eta_2$ /(GPa·d)	Displacement at Point 1 /mm	Displacement at Point 2 /mm	Displacement at Point 3 /mm	Displacement at Point 4 /mm	Displacement at Point 5 /mm
1	2.69	36.80	0.80	16.38	93.71	7.31	9.11	13.11	27.94	11.50
2	2.69	41.80	1.30	21.38	98.71	12.51	15.59	22.43	47.80	19.67
3	2.69	46.80	1.80	26.38	103.71	11.02	13.74	19.76	42.11	17.33
4	2.69	51.80	2.30	31.38	108.71	9.84	12.27	17.64	37.60	15.47
5	2.69	56.80	2.80	37.38	113.71	8.90	11.09	15.95	34.00	13.99
6	2.24	36.80	1.30	26.38	108.71	15.83	19.73	25.85	33.66	22.41
7	2.24	41.80	1.80	31.38	113.71	14.31	17.84	23.37	30.43	20.26
8	2.24	46.80	2.30	37.38	93.71	11.76	14.66	19.21	25.01	16.65
9	2.24	51.80	2.80	16.38	98.71	17.73	22.10	28.95	37.70	25.10
10	2.24	56.80	0.80	21.38	103.71	10.91	13.60	17.82	23.20	15.45
11	1.49	36.80	1.80	37.38	98.71	10.60	13.21	18.74	30.89	16.44
12	1.49	41.80	2.30	16.38	103.71	8.71	10.85	15.40	25.38	13.51
13	1.49	46.80	2.80	21.38	108.71	14.90	18.57	26.35	43.43	23.11
14	1.49	51.80	0.80	26.38	113.71	13.13	16.36	23.22	38.26	20.36
15	1.49	56.80	1.30	31.38	93.71	11.72	14.61	20.73	34.16	18.18
16	1.11	36.80	2.30	21.38	113.71	23.73	28.05	40.76	51.49	34.56
17	1.11	41.80	2.80	26.38	93.71	20.91	24.71	35.91	45.37	30.45
18	1.11	46.80	0.80	31.38	98.71	18.67	22.07	32.06	40.51	27.19
19	1.11	51.80	1.30	37.38	103.71	16.88	19.95	28.99	36.62	24.58
20	1.11	56.80	1.80	16.38	108.71	13.87	16.39	23.82	30.09	20.20
21	1.73	36.80	2.80	31.38	103.71	18.26	21.85	25.08	31.69	21.27
22	1.73	41.80	0.80	37.38	108.71	16.31	19.51	18.12	22.89	15.37
23	1.73	46.80	1.30	16.38	113.71	14.74	17.64	16.39	20.70	13.89
24	1.73	51.80	1.80	21.38	93.71	12.12	14.49	13.46	17.01	11.42
25	1.73	56.80	2.30	26.38	98.71	20.73	24.80	33.23	41.46	28.48

Section K143 + 621 was chosen for numerical simulation. Its buried depth was 646 m, we set the size of the model as long  $\times$  wide = 360 m  $\times$  150 m, the fixed end restraint was set at the bottom, the overlying pressure ( $\gamma H = 33.6 \text{ KN/m}^3 \times (646 - 150) \text{ m} = 16.67 \text{ MPa}$ ) was added above the model, the horizontal stress (8.3 MPa) was added on both sides of the model, and the surrounding rock masses all adopted the M-C failure criterion, as shown in Figure 17. The physical parameters of the surrounding rock mass, dominated by sericite and carbonaceous phyllite, were: average density  $\rho = 3.42 \text{ g/cm}^3$ , average elastic modulus  $E = 5.52 \text{ GPa}$ , Poisson ratio  $\nu = 0.38$ , internal cohesion  $c = 175 \text{ kPa}$ , internal friction angle  $\varphi = 27^\circ$ .

Using the BP neural network toolkit in MATLAB, the forward training of the rock mass parameters and deformation at Point 4 (Table 7) was performed, which produced the neural network model of Point 4, referred to as net4. Similarly, the training samples for the other point were generated and so were their neural network models, namely net1, net2, net3, and net5, respectively. Finally, the deformation measured at each point was input into the corresponding neural network model and the surrounding rock mass parameters were inverted. For the purpose of validation, the inverted mechanical parameters of the

surrounding rock mass were substituted into the Midas numerical model to determine the deformation at each point of the surrounding rock mass (Table 9).

**Table 9.** Parameter inversion of surrounding rock mass and error analysis.

Monitoring Point	Measured Deformation /mm	Output: Inverted Mechanical Parameters of the Surrounding Rock Mass					Simulated Deformation /mm	Relative Error /%
		$E_0$ /GPa	$\sigma_r$ /MPa	$E_1$ /GPa	$\eta_1$ /(GPa·d)	$\eta_2$ /(GPa·d)		
1	23.73	3.44	35.35	0.92	16.85	104.49	26.67	12.37
2	28.05	2.91	31.89	0.81	12.39	97.20	30.69	9.41
3	40.76	2.12	21.67	0.59	10.01	9.13	45.57	11.81
4	51.50	1.71	16.91	0.48	9.19	8.11	58.54	13.67
5	34.56	2.39	22.63	0.71	11.15	88.00	37.51	8.53

The relative error between the measured displacement and the numerically simulated displacement obtained through inversion was within 15%, indicating the good consistency and high applicability of the proposed method. Therefore, one can build a monitoring system for the largely-deformed surrounding rock mass section, according to the on-site information (such as the lithology combination, underground water status, bedding thickness, rock mass texture, surrounding rock mass integrity, maximum principal stress, and on-site measured rock deformation) for the purposes of gaining real-time information of the tunnel's surrounding rock mass parameter, adjusting the support plan in a timely manner, and providing references for design and construction.

## 5. Conclusions

Due to the concealment of tunnel engineering, it is difficult to obtain the parameters of the surrounding rock mass after excavation. In this study, we combined the traditional Nashihara model with the Hoek–Brown failure criterion and developed the creep constitutive model for the jointed rock mass. Then, the creep parameters of the surrounding rock mass of the Ganbao tunnel were inverted and validated by integrating the on-site monitoring and the BP neural network. The following conclusions were drawn:

- (1) By reviewing the typical cases of large deformation in soft rock tunnels, the main influential factors can be summarized as the lithology combination, weathering effect, and underground water status. With the classical rock mass failure criterion, it is hard to thoroughly incorporate the geological characteristics of the actual rock mass and therefore the semi-empirical semi-theoretical Hoek–Brown approach is more fit-for-purpose.
- (2) The geological characteristics of the engineering rock mass were quantitatively characterized using two indexes, namely, the rock mass block index (*RBI*) and the absolute weathering index (*AWI*). Following the Hoek–Brown criterion, the long-term strength  $\sigma_r$  and elastic modulus  $E_0$  of the rock were obtained and then substituted into the rock mass creep constitutive model based on the Nashihara model and the Hoek–Brown failure criterion. By doing so, the original five creep parameters that needed to be determined in the creep equation were reduced to three, which simplifies the calculation of the constitutive model, while well reflecting the engineering, geological, and creep characteristics of the rock mass on site.
- (3) Considering the fact that the actual engineering geology varies at different positions of the tunnel's surrounding rock mass, a specific BP neural network model was built for each monitoring point. Then, the rock mass parameters at each point were inverted from the on-site measured deformation. At last, the inverted parameters were input into the numerical model to calculate the deformation at each point, which was compared with the corresponding measured deformation. The resultant errors

were all within 15%, satisfying the engineering requirements and demonstrating the reliability of the proposed method.

- (4) The values of the rock mass *GSI* (Figure 2) were all determined according to the engineering geology handbook, relevant standards, and existing literature. Therefore, these values can be adjusted as per the field condition. The inversion of the surrounding rock mass parameters is highly affected by the basic parameters of the engineering geological characteristics and the in-situ stress field of the tunnel's surrounding rock mass. Hence, during applications of the proposed method, the basic parameters need to be accurately measured to improve the accuracy of the inversion.
- (5) This method is suitable for tunneling in unsupported rock mass or plainly supported tunnels after excavation.

**Author Contributions:** Writing—original draft preparation, C.C.; writing—review and editing, T.L.; methodology, C.M.; investigation, H.Z.; software, J.T.; data curation, Y.Z.; funding acquisition, T.L. All authors have read and agreed to the published version of the manuscript.

**Funding:** This research was funded by National Natural Science Foundation of China, grant number U19A20111.

**Institutional Review Board Statement:** Not involved.

**Informed Consent Statement:** Not involved.

**Data Availability Statement:** The study did not report any data.

**Acknowledgments:** This work was supported by the National Natural Science Foundation of China (NO. U19A20111). The financial support is gratefully acknowledged. Special thanks are due to Tianbin Li and Chunchi Ma for their help in improving this article.

**Conflicts of Interest:** The authors declare no conflict of interest.

## References

1. He, M.; Jing, H.; Sun, X. *Mechanics of Soft Rock Engineering*; Science Press: Beijing, China, 2002.
2. Kong, P.; Jiang, L.S.; Shu, J.M.; Sainoki, A.; Wang, Q.B. Effect of fracture heterogeneity on rock mass stability in a highly heterogeneous underground roadway. *Rock Mech. Rock Eng.* **2019**, *52*, 4547–4564. [[CrossRef](#)]
3. Chen, Z.; He, C.; Xu, G.; Ma, G.; Wu, D. A case study on the asymmetric deformation characteristics and mechanical behavior of deep-buried tunnel in phyllite. *Rock Mech. Rock Eng.* **2019**, *52*, 4527–4545. [[CrossRef](#)]
4. Jia, P.; Tang, C.; Yang, T.; Wang, S. Numerical Stability Analysis of Surrounding rock mass Mass Layered by Structural Planes with Different Obliquities. *J. Northeast Univ.* **2006**, *27*, 1275–1278.
5. Li, L.; Guan, J.; Xiao, M.; Liu, H.; Tang, K. A creep constitutive model for transversely isotropic rocks. *Rock Soil Mech.* **2020**, *41*, 2922–2930, 2942.
6. Li, C.; Wang, J.; Xie, H. Anisotropic creep characteristics and mechanism of shale under elevated deviatoric stress. *J. Pet. Sci. Eng.* **2020**, *185*, 106670. [[CrossRef](#)]
7. Li, A.; Xu, N.; Dai, F.; Gu, G.; Hu, Z.; Liu, Y. Stability analysis and failure mechanism of the steeply inclined bedded rock masses surrounding a large underground opening. *Tunn. Undergr. Space Technol.* **2018**, *77*, 45–58. [[CrossRef](#)]
8. Song, D.; Chen, J.; Cai, J. Deformation monitoring of rock slope with weak bedding structural plane subject to tunnel excavation. *Arab. J. Geosci.* **2018**, *11*, 251. [[CrossRef](#)]
9. Gao, F.; Guo, J. Stress mechanism and deformation monitoring of bias tunnel. *Int. J. Simul. Syst. Sci. Technol.* **2016**, *17*, 14.1–14.4. [[CrossRef](#)]
10. Yin, C.; Li, H.; Che, F.; Li, Y.; Hu, Z.; Liu, D. Susceptibility mapping and zoning of highway landslide disasters in China. *PLoS ONE* **2020**, *15*, e0235780. [[CrossRef](#)]
11. Liu, C.H.; Li, Y.Z. Analytical study of the mechanical behavior of fully grouted bolts in bedding rock slopes. *Rock Mech. Rock Eng.* **2017**, *50*, 2413–2423. [[CrossRef](#)]
12. Vergara, M.R.; Kudella, P.; Triantafyllidis, T. Large scale tests on jointed and bedded rocks under multi-stage triaxial compression and direct shear. *Rock Mech. Rock Eng.* **2015**, *48*, 75–92. [[CrossRef](#)]
13. Li, L.; Tan, Z.S.; Guo, X.L.; Wu, Y.; Luo, N. Large deformation of tunnels in steep dip strata of interbedding phyllite under high geostresses. *Chin. J. Rock Mech. Eng.* **2017**, *36*, 1611–1622.
14. Li, X.H.; Xia, B.W.; Li, D.; Han, C.R. Deformation characteristics analysis of layered rockmass in deep buried tunnel. *Rock Soil Mech.* **2010**, *31*, 1163–1167.
15. Fu, X. *Numerical Simulation of Asymmetric Large-Deformation Energy-Releasing Bolt Support for Layered Soft Rock Tunnel*; Chengdu University of Technology: Chengdu, China, 2020.

16. Li, Z.; Shan, R.; Wang, C.; Yuan, H.; Wei, Y. Study on the distribution law of stress deviator below the floor of a goaf. *Geomech. Eng.* **2020**, *21*, 301–313. [[CrossRef](#)]
17. Tian, M.; Han, L.; Meng, Q.; Ma, C.; Zong, Y.; Mao, P. Physical model experiment of surrounding rock mass failure mechanism for the roadway under deviatoric pressure form mining disturbance. *KSCE J. Civ. Eng.* **2020**, *24*, 1103–1115. [[CrossRef](#)]
18. Wang, Z.-J.; Luo, Y.-S.; Guo, H.; Tian, H. Effects of initial deviatoric stress ratios on dynamic shear modulus and damping ratio of undisturbed loess in China. *Eng. Geol.* **2012**, *143–144*, 43–50. [[CrossRef](#)]
19. Kroon, M.; Faleskog, J. Numerical implementation of a J2 and J3 dependent plasticity model based on a spectral decomposition of the stress deviator. *Comput. Mech.* **2013**, *52*, 1059–1070. [[CrossRef](#)]
20. Wang, Q.; Pan, R.; Jiang, B.; Li, S.; He, M.; Sun, H.; Wang, L.; Qin, Q.; Yu, H.; Luan, Y. Study on failure mechanism of roadway with soft rock in deep coal mine and confined concrete support system. *Eng. Fail. Anal.* **2017**, *81*, 155–177. [[CrossRef](#)]
21. Wang, W.; Zhang, C.; Wei, S.; Zhang, X.; Guo, S. Whole section anchor-grouting reinforcement technology and its application in underground roadways with loose and fractured surrounding rock mass. *Tunn. Undergr. Space Technol.* **2016**, *51*, 133–143. [[CrossRef](#)]
22. Xu, G.; He, C.; Chen, Z.; Yang, Q. Transversely isotropic creep behavior of phyllite and its influence on the long-term safety of the secondary lining of tunnels. *Eng. Geol.* **2020**, *278*, 105834. [[CrossRef](#)]
23. Li, X.; Ju, M.; Yao, Q.; Zhou, J.; Chong, Z. Numerical investigation of the effect of the location of critical rock block fracture on crack evolution in a gob-side filling wall. *Rock Mech. Rock Eng.* **2016**, *49*, 1041–1058. [[CrossRef](#)]
24. Zhou, J.; Wei, Q.; Liu, G. Back analysis on rock mechanics parameters for highway tunnel by BP neural network method. *Chin. J. Rock Mech. Eng.* **2004**, *23*, 941–945.
25. Cao, W.; Jiang, Y.; Sakaguchi, O.; Li, N.; Han, W. Predication of Displacement of Tunnel Rock Mass Based on the Back-Analysis Method-BP Neural Network. *Geotech. Geol. Eng.* **2021**, *2021*, 1–14. [[CrossRef](#)]
26. Wu, Q.; Yan, B.; Zhang, C.; Wang, L.; Ning, G.; Yu, B. Displacement prediction of tunnel surrounding rock mass: A comparison of support vector machine and artificial neural network. *Math. Probl. Eng.* **2014**, *2014*, 351496. [[CrossRef](#)]
27. Deng, X.; Xu, T.; Wang, R. Risk evaluation model of highway tunnel portal construction based on BP fuzzy neural network. *Comput. Intell. Neurosci.* **2018**, *2018*, 8547313. [[CrossRef](#)]
28. Wen, H.; Yin, J.; Qin, Z.; Xie, R. Application of BP Neural Network to the Back Analysis of Mechanical Parameters of Tunnel Surrounding rock mass. *J. Yangtze River Sci. Res. Inst.* **2013**, *30*, 47–51, 56.
29. He, Y.; Sun, X.; Zhang, Y.; Guo, H.; Li, Q. Intelligent fusion model and analysis method for rock parameter inversion of water diversion tunnel. *J. Hydroelectr. Eng.* **2021**, *40*, 114–126.
30. Ma, F.; Jia, S. Back analysis of elastoplastic parameters of surrounding rock mass for roadway in mudstone and its long-term stability prediction. *Rock Soil Mech.* **2014**, *7*, 1987–1994.
31. Amadei, B. Strength of a regularly jointed rock mass under biaxial and axisymmetric loading conditions. *Int. J. Rock Mech. Min. Sci. Geomech. Abstr.* **1988**, *25*, 3–13. [[CrossRef](#)]
32. Xiao, S.; Yang, S. *Rock Mass Mechanics*; Geological Publishing House: Beijing, China, 1987.
33. Hoek, E.; Brown, E.T. Practical estimates of rock mass strength. *Int. J. Rock Mech. Min. Sci.* **1997**, *34*, 1165–1186. [[CrossRef](#)]
34. Marinos, P.; Hoek, E. Estimating the geotechnical properties of heterogeneous rock masses such as flysch. *Bull. Eng. Geol. Environ.* **2001**, *60*, 85–92. [[CrossRef](#)]
35. Hoek, E.; Brown, E.T. The Hoek–Brown failure criterion and GSI–2018 edition. *J. Rock Mech. Geotech. Eng.* **2019**, *11*, 445–463. [[CrossRef](#)]
36. Hu, X.; Zhong, P.; Ren, Z. Rock-mass block index and its engineering practice significance. *J. Hydraul. Eng.* **2002**, *33*, 80–83.
37. Parker, A. An index of weathering for silicate rocks. *Geol. Mag.* **1970**, *107*, 501–504. [[CrossRef](#)]
38. Su, Y.; Feng, L.; Li, Z.; Zhao, M. Quantification of elements for geological strength index in Hoek–Brown criterion. *Chin. J. Rock Mech. Eng.* **2009**, *28*, 36–43.
39. Li, R.; Wu, L. Research on characteristic indexes of weathering intensity of rocks. *Chin. J. Rock Mech. Eng.* **2004**, *23*, 3830.